1 # Carbon emissions and radiative forcings from tundra wildfires
2 # in the Yukon-Kuskokwim River Delta, Alaska

3 Michael Moubarak[1], Seeta Sistla[2], Stefano Potter[3], Susan M. Natali[3,*], Brendan M. Rogers[3,*]
4 [1]Department of Biology, Hamilton College, Clinton, NY 13323, United States
5 [2]Department of Natural Resources and Environmental Sciences, California Polytechnic State University, San Luis
6 Obispo, CA 93407, United States
7 [3]Woodwell Climate Research Center, Falmouth, MA 02540, United States
8
9 *Correspondence to:* Michael Moubarak (moubarak.michael@gmail.com)
10 *Equal last authorship

Abstract

34   Tundra environments are experiencing elevated levels of wildfire, and the frequency is expected to keep

35   increasing due to accelerating climate change in the Arctic. Tundra wildfires can release globally significant

36   amounts of greenhouse gasses that influence the Earth's radiative balance. Here we develop a novel method for

37   estimating carbon loss and the resulting radiative forcings of gaseous and aerosol emissions from 2015 tundra

38   wildfires in the Yukon-Kuskokwim Delta (YKD), AK. We paired burn depth measurements using two vegetative

39   reference points that survived the fire event —*Sphagnum fuscum* and *Dicranum spp.*— with measurements of local

40   organic matter and soil carbon properties to estimate total ecosystem organic matter and carbon loss. We used

41   remotely-sensed data of fire severity from Landsat 8 to scale our measured losses to the entire fire-affected area,

42   with an estimated total loss of 2.04 Tg of organic matter and 0.91 Tg of carbon, and an average loss of 3.76 kg m^{-2}

43   of organic matter and 1.68 kg m^{-2} of carbon in the 2015 YKD wildfires. To demonstrate the impact of these fires on

44   Earth's radiation budget, we developed a simple but comprehensive framework to estimate the radiative forcing

45   from Arctic wildfires. We synthesized existing research on the lifetime and radiative forcings of gaseous and

46   aerosol emissions of CO_2, N_2O, CH_4, O_3 and its precursors, and fire aerosols. The model shows a net positive

47   cumulative mean radiative forcing of 3.67 W m^{-2} using RCP 4.5 and 3.37 W m^{-2} using RCP 8.5 at 80 years post-fire,

48   which was dominated by CO_2 emissions. Our results highlight the climate impact of tundra wildfires, which

49   positively reinforce climate warming and increased fire frequency through the radiative forcings of their gaseous

50   emissions.

1 Introduction

51

52   The Arctic region is characterized by permafrost soils with low rates of decomposition and high carbon

53   content from millennia of positive net ecosystem production (NEP; Lindgren et al., 2018). As a result, there is more

54   than twice as much carbon stored in permafrost soils as there is in the atmosphere, including roughly 1,035 ± 150 Pg

55   of carbon in the top three meters of soil (Schuur et al., 2015). Surface air temperatures in the Arctic have been

56   increasing more than twice as fast as the global average since the mid-20th century (Cohen et al., 2018) and are

57   expected to continue increasing with more variable precipitation (IPCC, 2021; Hu et al., 2015). Changing

58   environmental conditions will place some of this large carbon stock at risk for release into the atmosphere through

59   increased biological activity and wildfire (Natali et al., 2019, Natali et al., 2015, Rocha et al., 2011a, Hu et al.,

60   2010).

61   Fires are an increasingly important component of tundra carbon cycling. Fires are becoming more frequent

62 in Arctic systems due to increasing occurrences of hot and dry conditions coupled with more lightning ignitions

63 (Chen et al., 2021, Bieniek et al., 2020, Veraverbeke et al., 2017). For example, the 2007 Anaktuvuk River megafire

64 on the North slope of Alaska occurred during an especially hot and dry period and released an amount of carbon

65 similar in magnitude to annual sequestration across the entire tundra biome (Mack et al., 2011). Continued and

66 potentially accelerated rates of warming are expected to further increase the frequency of tundra wildfires, thereby

67 releasing significant amounts of carbon and altering the net carbon balance of the tundra biome (Hu et al., 2015).

68   A recent body of literature indicates the potential to estimate wildfire carbon emissions in boreal forests by

69 linking geospatial predictors, most prominently satellite-derived estimates of fire severity and extent, with *in situ*

70 measurements of carbon loss (e.g. Dieleman et al., 2020, Walker et al., 2018b, Veraverbeke et al., 2015, and Rogers

71 et al., 2014). Despite increasing incidence of tundra wildfires, these studies have primarily focused on boreal forests,

72 and few estimates are available for tundra (Mack et al., 2011). Whereas satellite-derived fire extent and severity is

73 widely available, representative *in situ* measurements of tundra wildfires are not. *In situ* measurements of fire

74 effects on tundra organic soils are challenging due to a lack of reference points (e.g., adventitious roots) that survive

75 the fire, which are used to estimate pre-fire organic matter depth and content (Walker et al., 2018a, Rogers et al.,

76 2014, Boby et al., 2010). Measurements of organic matter loss must also be region-specific because of differences

77 in vegetation and soil properties (Walker et al., 2020c, Mack et al., 2011).

78   Although carbon loss estimates from Arctic wildfires are important for understanding the impacts of

79 climate change on carbon budgets, radiative forcings from wildfire gaseous and aerosol emissions are needed to

80 properly gauge the impact on the Earth's atmosphere and climate (Huang et al., 2016, Ward et al., 2012, Randerson

81 et al., 2006). Radiative forcings from wildfires depend spatially on fire severity and atmospheric conditions and

82 temporally on changing atmospheric background concentrations in the months, years, and decades following the fire

83 (Huang et al., 2016, Joos et al., 2013). To date, radiative forcings from high-latitude wildfires have been estimated

84 for particular boreal forests (Huang et al., 2016, O'Halloran et al., 2012, Randerson et al., 2006) and within global

85 models (Ward et al., 2012), but not for tundra ecosystems.

86   Here we take a two-step approach to assess the impact of tundra wildfires on carbon budgets and climate.

87 We first developed a method for measuring carbon loss *in situ* in tundra ecosystems, particularly for the 2015 fire

88 season in the Yukon-Kuskokwim Delta, AK. We tested the agreement of multiple pre-fire reference points for

89   estimating burn depth in the field, and combined these estimates with laboratory-measured organic matter and

90   carbon fractions to estimate emissions. We then used 30 m remotely-sensed fire severity data (differenced

91   Normalized Burn Ratio, or dNBR) from Landsat 8 to scale our measurements to the entire fire area. Finally, we

92   estimated the long-term radiative forcings of the fire's gaseous and particulate emissions, including long-lived

93   greenhouse gasses, ozone, ozone precursors, and aerosols, using a variety of published algorithms and arctic-specific

94   parameters when available.

95   **2 Materials and Methods**

96   **2.1 Study Area**

97   Field measurements were collected in the summer of 2019 in a burn scar from the 2015 fire season in the

98   Yukon-Kuskokwim Delta, AK (YKD) (Fig. 1). Base camp was situated at 61.2632 ºN, 163.2458 ºW, approximately

99   95 kilometers northwest of Bethel, AK, accessible by float plane and helicopter. Sampling was done within about

100   an 11-kilometer radius of the base camp (Fig. 1c). Measurements from the field were scaled to all fire scars in the

101   YKD that burned in 2015 (Fig 1b).

102

Figure 1. (a) The location of the YKD within Alaska, (b) the areas of fires in 2015 within the YKD, and (c) the locations of our vegetative reference point height transects in burned and unburned areas within about an 11 km radius from base camp. Sources: Esri, DigitalGlobe, GeoEye, i-cubed, USDA FSA, USGS, AEX, Getmapping, Aerogrid, IGN, IGP, swisstopo, and the GIS User Community.

The YKD contains tussock-sedge, dwarf-shrub, and lichen and moss tundra communities over ice-rich

permafrost peat plateaus (Raynolds et al., 2005). These peat plateaus were the primary land component burned in

the wildfires and were separated by fens, bogs, and open water. Within our sample area, lichen was the dominant

vegetation type (Frost et al., 2020), shrubs were interspersed across the landscape, and tussocks were rare. Soil is

predominantly organic (Jorgenson et al., 2000), which has accumulated over sand deposits from the Pleistocene

period (Shaw, 1998).

2.2 Vegetative marker height measurements

We measured the height of vegetative reference points above the surface in both unburned and burned

areas. Three main dominant surface vegetative reference points were available: *Sphagnum fuscum, Dicranum spp.,*

and *Eriophorum vaginatum* (tussocks; similar to the methods of Mack et al. (2011)). *S. fuscum* moss appeared in

119   large mats. *Dicranum* moss appeared in small dense patches. All vegetative reference points were particularly

120   conspicuous in burned areas as they were elevated above the burned surface (Fig. 2). In the burned area, we

121   measured the distance from the soil surface to top of the living parts of the vegetative reference points, which we

122   assumed to indicate full survival in the fire event. We did not measure dead remnants of vegetative reference points,

123   because we expect that these may not represent the actual pre-fire vegetation height.

124
125   **Figure 2.** An example burn depth measurement from the surviving top of a *Dicranum spp.* moss patch (red arrow;
126   pink string) to the top of the soil (blue arrow) in a burned transect. Transect tape was used to measure distance
127   between the moss patches.
128
129   We measured the average height along a transect between two like reference points. At the highest living

130   point on each moss patch, or to the top of the corms at the base of a tussock, we inserted a nail (red arrow, Fig. 2).

131   We ran a taut piece of string between the two nails (Fig. A1). In between the edges of the moss patch or tussock

132   pair (Fig. A1), we took height measurements vertically from the string to the ground, which was soil in the burned

133   areas (blue arrow, Fig. 2) or a dense vegetative surface in the unburned areas (Fig. A2). In between the starting

134   ending point measurements on the transect we recorded height every 25 centimeters (Figs. A2 and A3). The starting

135   and ending points were never greater than 50 centimeters from the nail. Latitude and longitude were recorded at all

136   transects with an accuracy of three meters (Fig. 1) for ground-truthing remotely sensed burn severity categories.

137   One potential source of error is post-fire subsidence between the vegetative reference point pairs that may

138   bias the relative height of a vegetative marker above the surface (Jones et al., 2015). We minimized this potential

139   bias by maintaining transect lengths less than four meters, and predominantly one to two meters in burned areas.

140   We also visually assessed the area between each vegetative marker for signs of subsidence including cracked soil or

141   large elevation differences and chose not to sample these areas. Measuring from the top of one vegetative marker to

142   the top of another marker controlled for slopes and larger landscape elevation features because the string largely

143   mimicked the angle of the landscape.

144   We selected transects for height measurements opportunistically in the burned and unburned areas.

145   However, we tried to maximize spatial separation between transects and target visually identifiable areas of varying

146   burn severity. We corrected for spatial autocorrelation biases between transect averages in our statistical analyses

147   (see below). In unburned areas we maximized the number of transects measured for each vegetative reference point,

148   *Sphagnum* (n = 38), *Dicranum* (n = 40), and *Eriophorum* (n = 19).

149   Each burn depth measurement was associated with a dNBR value based on the 30 m pixel containing its

150   centroid. Burn depth measurements that came from the lowest third, middle third, and upper third of dNBR values

151   were considered to be in low, moderate, and high severity burned areas, respectively and a roughly even numbers of

152   transects were sampled in each burn severity category for *Sphagnum* (n = 56: high n = 20, med n = 17, low n = 19),

153   *Dicranum* (n = 54: high n = 18, med n = 17, low n = 19), and *Eriophorum* (n = 24: high n = 7, med n = 11, low n =

154   6).

155   **2.3 Organic matter and carbon pool measurements**

156   We calculated the total ecosystem organic matter and carbon pool sizes in unburned areas surrounding the

157   fire scar. We took vegetation and soil samples together in cores using a hand drill and hollow metal drill bit that was

158   30 centimeters in length and six centimeters in diameter. Cores were extracted at three points (start, middle, and

159   end) along transects between like vegetative reference points. We selected four sites of less than half a hectare

160   surrounding areas where we took our unburned vegetative reference point height measurements. These sites were

161   selected opportunistically to ensure the presence of an appropriate number of each of the three vegetative reference

162   points. In each site, we extracted cores from three transects per vegetative reference point pair, which totaled 27 soil

163   cores per site. In one site we found only two tussock pairs, so our total number of samples was 105. We maximized

164   physical separation of the unburned sites to control for heterogeneity in local soil and vegetation characteristics.

165   We measured the height of the live vegetation layer and fibric soil horizons for each core. Vegetation

166   layers and soil horizons were identified visually by soil density, texture, color, and identifiable plant parts. Each

167   core was separated into vegetation and fibric soil layers that were homogenized, weighed, and subsampled in the

168   field, and subsequently stored frozen until analyzed. In the lab, each vegetation sample and approximately 15 grams

169   of each fibric sample were dried for 48 hours at 60 ℃ and weighed to determine soil water content. We used the

170   proportion of dry mass to wet mass to estimate the dry weight of the field sample, which was used to determine bulk

171   density (g dry mass cm^{-3}). Soil samples were combusted for five hours at 450 ℃ to determine organic matter

172   content and analyzed for percent carbon using an Elementar Vario Max CN analyzer at the Woodwell Climate

173   Research Center, Falmouth, MA. We assumed the dry mass of the vegetation layer was fully organic matter. Using

174   the average across all herbaceous plant organs, we assumed the carbon content of the vegetation layer was 43.04%

175   from Ma et al. (2018). To calculate organic matter and carbon pools (kg m^{-2}) for each organic soil sample, we

176   multiplied bulk density by the height of the layer and percent organic matter or percent carbon, respectively. These

177   values were normalized for each sample to the average depth of the vegetation layer, which was seven centimeters,

178   and 10 centimeters in the fibric horizon.

179   **2.4 Fire severity**

180   We used a remotely sensed metric of fire severity from Landsat 8 Tier 1 surface reflectance imagery: the

181   Difference Normalized Burn Ratio (dNBR; Eq. 1; Key and Benson, 2006), which is based on the Normalized Burn

182   Ratio (NBR; Eq. 2). Clouds, cloud shadows and snow were masked from all images using the provided pixel quality

183   attributes generated from the CFMASK algorithm. Imagery for this index was acquired as the mean Landsat 8

184   composite between June 1st and August 31st for one year pre- and one year post-fire, and for all fire scars. All

185   remotely sensed variables were extracted in Google Earth Engine (Gorelick et al., 2017).

186    $dNBR = (NBR_{prefire} - NBR_{postfire}) \times 1000,$ (1)

187    $NBR = \frac{(NIR - SWIR)}{(SWIR + NIR)},$ (2)

188   Where in Eq. (2) NIR is near-infrared (Band 5) and SWIR is shortwave infrared (Band 7).

189   **2.5 Calculating final estimates**

190   We calculated organic matter combustion and carbon loss across the fire area using burn depth derived

191   from the moss reference points (Fig. A4). We excluded estimates derived from tussock measurements because burn

192   depth estimates from tussocks correlated negatively with remotely sensed fire severity. Moreover, our sample size of

193 tussock-based measurements was substantially lower than the moss vegetative reference points due to their

194 infrequent occurrence in our study domain (Frost et al., 2020). Excluding tussock measurements required

195 reassigning dNBR values evenly as before across only *Dicranum* (n = 54: high n = 18, med n = 18, low n = 18) and

196 *Sphagnum* (n = 56: high n = 20, med n = 18, low n = 18) reference points. The highest dNBR values in the low and

197 moderate severity categories became the threshold values for low to moderate and moderate to high severity burn,

198 respectively. We split the fire area, based on these thresholds, into the three categories for burn severity. There

199 were 130.01 km^2 of low severity burn, 85.16 km^2 of moderate severity burn, and 326.37 km^2 of high severity burn,

200 which summed to 541.54 km^2 of total fire area (Fig. A5).

201   For final analysis of organic matter and carbon loss, we averaged the height of *Sphagnum* and *Dicranum*

202 reference points in the unburned areas to determine one height for each reference point, since their respective

203 heights were statistically different (p < 0.001). Burn depth was calculated at each transect in the burned areas by

204 subtracting the standard unburned height from the transect average height. We also averaged the dry organic matter

205 and carbon pool within the vegetative layer and fibric horizon separately across *Sphagnum* and *Dicranum* reference

206 points to determine one pool size for our sampling area.

207   Average organic matter or carbon loss (kg m^{-2}) was estimated as the product of the organic matter or carbon

208 concentrations and depth of the vegetation and soil that burned at each burn depth transect. Average loss at each

209 transect was the sum of loss from each horizon. For our final calculation of total dry organic matter and carbon loss,

210 we averaged the organic matter and carbon lost across transects for *Sphagnum* and *Dicranum* reference points within

211 each fire severity category. Over the landscape, total carbon or organic matter released was calculated by

212 multiplying average carbon or organic matter loss for a given burn severity category by the total burned area for that

213 category. Total carbon or organic matter released was then calculated as the sum from all three burn severity

214 categories.

215 **2.6 Radiocarbon**

216   We used radiocarbon dating to confirm our burn depth measurements by comparing the radiocarbon age of

217 *Sphagnum* macrofossils on the burned soil surface with the radiocarbon age of *Sphagnum* macrofossils at different

218 depths of the unburned soil profile, similar to the methods of Mack et al. (2011). In the field we extracted one

219 unburned core and three burned cores of the same dimensions as our primary soil cores, described above. We

220 extracted a one-centimeter thick subsample of the cores every five centimeters in depth and froze the samples in a

221 sealed plastic bag until lab analysis. To construct an age profile, we analyzed unburned cores at depths of five to 20

222 centimeters for radiocarbon age. We assumed that a depth of zero centimeters had carbon from the time of harvest

223 in 2019. In the burned cores, we analyzed the zero-centimeter depth (i.e., surface) for radiocarbon.

224   In the lab, we visually identified *Sphagnum* branches in each of the subsamples being tested and rinsed

225 them with deionized water. The branches were then dried for 48 hours at 60 ºC, and roughly five milligrams of dry

226 branch matter per sample was sent to the W.M. Keck Carbon Cycle Accelerator Mass Spectrometry Laboratory at

227 the University of California Irvine for the ^{14}C content and δ^{13}C. Results for ^{14}C analysis are reported as the fraction

228 modern, which is defined as the ratio of the sample's carbon isotope ratio to that of a standard (Reimer, 2004).

229 Fraction modern values are calibrated to calendar years using OxCal online 4.4.1 (Ramsey, 2009), with the

230 appropriate modern era bomb curve taken from Hua et al. (2013). Due to the shape of the bomb curve, there are at

231 least two possible calendar years in which the carbon in the sample was fixed. However, we did not use the oldest

232 age for unburned samples with multiple calendar ages because the age of these samples must increase with depth

233 (Walker et al., 2019, Mack et al., 2011), which is not supported when considering the oldest calendar ages.

234 Furthermore, we were confident the burned samples were from the younger age because they were from visually

235 shallow burn depths. We compared the calendar age of carbon at the burned soil surface to age by depth profile

236 taken from the unburned core.

2.7 Radiative forcings model

238   We created a temporally-explicit model of radiative forcings for gaseous and aerosol emissions of tundra

239 wildfires and used it to compute the radiative forcings per unit burned area, similar to the framework employed in

240 Randerson et al. (2006) and Huang et al. (2016). These equations were derived using the average amount of organic

241 matter lost across fire-wide burn severity classes and vegetative reference points. Our model included the long-lived

242 greenhouse gas species CO_2, CH_4, and N_2O, as well as short-lived climate forcers, tropospheric O_3, O_3 precursors,

243 and aerosols. Ozone precursors include NO_x, nonmethanogenic volatile organic carbons (NMVOCs), and CO.

244   We first used emissions factors from Akagi et al. (2011) to calculate the mass of gaseous and aerosol

245 emissions from our estimated organic matter losses. Emission factors have not been previously defined for tundra

246 burning. Given that boreal forest, whose definition for emission factors includes organic soils, peat, and woody

247 vegetation, is likely the closest ecosystem type in terms of fuel properties to tundra in Akagi et al. (2011), we

248 employed these emission factors. However, we note a possible overestimate of relative contribution from woody

249 vegetation emissions in these numbers due to the relative lack of woody vegetation on the tundra landscape. We

250 converted the mass of each emission to a volume as the molar fraction of the emission to the atmosphere.

251   Once we estimated the mass of each gaseous emission, we calculated the concentration of the gas

252 remaining in the atmosphere and its radiative forcing each year after the fire by synthesizing existing models and

253 research on the lifetimes and radiative forcings of these gaseous emissions. Our calculations of radiative forcing

254 were dependent on the future ambient concentration of greenhouse gasses in the atmosphere. As a result, we

255 calculated the radiative forcings of gaseous emissions for three scenarios: historic, representative concentration

256 pathway (RCP) 4.5, and RCP 8.5. The historic scenario assumes the ambient concentration of greenhouse gasses

257 remains constant in the atmosphere after the fire. Future atmospheric concentrations for each RCP were taken from

258 Meinshausen et al. (2011). The radiative forcing for each gaseous emission per year was calculated separately and

259 then summed across forcing agent. Since O_3 precursors and aerosols had the most uncertain lifetimes and radiative

260 forcings (Bond et al., 2011, Quinn et al., 2008), we calculated the total radiative forcing of the emissions with and

261 without them. A flowchart of our general methodology for the entire radiative forcings calculation is presented in

262 the supplemental information (Fig. A6).

263 **2.8 Methane and Nitrous Oxide**

264   Our radiative forcing calculations for CH_4 and N_2O were based on Ward et al. (2012). For both gasses, we

265 assumed a pulse emission and calculated the concentration remaining in each year after the fire using a simple box

266 model with one outflow as shown in Eq. (3), where C_o is the initial pulse mass of the gas, t is the number of years

267 after the fire, and L is the lifetime of the gas.

268 $C = C_o e^{\frac{-t}{L}},$ (3)

269 $L = L_o \left(\frac{E}{E_t}\right)^{-0.05},$ (4)

270

271   We used the atmospheric lifetimes for both gasses reported in Myhre et al. (2013). However, we calculated

272 a decreased lifetime of N_2O using Eq. (4) from Ward et al. (2012), as its ambient concentration changed in future

273 emissions scenarios, where L_o is the initial lifetime of N_2O from Myhre et al. (2013), E is the ambient concentration

274 of N_2O in the year the fire burned, and E_t is the ambient concentration of N_2O at each year after the fire based on the

275 future emissions scenario (Meinshausen et al., 2011). We did not account for the effect of the changing atmospheric

276 concentration on the lifetime of N_2O due to the pulse emission itself.

277   We then calculated the perturbation concentrations of CH_4 and N_2O in the atmosphere each year after the

278   fire as the sum of the remaining pulse emissions and the ambient concentrations and used Eqs. (5) and (6) from

279   Ward et al. (2012) to estimate the radiative forcing of both gasses.

280    $RF = 0.036\left(\sqrt{M} - \sqrt{M_o}\right) - [f(M, N_o) - f(M_o, N_o)],$ (5)
281    $f(M, N) = 0.47 ln[1 + 2.01 \times 10^{-5}(MN)^{0.75} + 5.31 \times 10^{-15}M(MN)^{1.52}],$ (6)
282
283   The radiative forcing of the gas at each year was RF, M was the perturbation concentration of the gas

284   whose radiative forcing was being calculated, and M_o and N_o were the ambient concentrations of both gasses

285   depending on which gas's radiative forcing was being calculated.

2.9 Carbon Dioxide

287   Carbon dioxide has a highly variable lifetime under different future emissions scenarios depending on the

288   strength of ocean and land sinks. To account for this variation, we used impulse response functions (IRFs) from

289   Joos et al. (2013), which represent the fraction of a pulse of CO_2 remaining in the atmosphere at each year after the

290   pulse for each scenario. For each year post-fire, we multiplied the relevant IRF function by the concentration of

291   CO_2 initially released to estimate the amount of CO_2 remaining in the atmosphere. The radiative forcing for CO_2

292   was calculated using Eq. (7) taken from Myhre et al. (1998), where C is the perturbation concentration and C_o is the

293   ambient concentration of the gas in each year.

294    $RF = 5.35 \ ln \left(\frac{C_o + C}{C_o} \right),$ (7)

2.10 Tropospheric Ozone

296   Tropospheric O_3 is created photochemically in the smoke plumes of wildfires by the combination of

297   sunlight and O_3 precursor gasses, and its creation can be expressed as a function of time and the amount of carbon

298   monoxide released (Jaffe and Wigder, 2012). We used data compiled in Jaffe and Widger (2012), who provided a

299   synthesis of O_3 and its relationship with CO for fire plumes sampled in the Arctic at various times after a fire to

300   calculate a mean plume lifetime and derive a linear relation between plume age and the ratio of O_3 to CO. Because

301   the average plume age sampled was five days, we assumed O_3 was created for five days after the fire. The

302   concentration of O_3 on each of those five days was calculated by multiplying the initial concentration of CO released

303   from the fire (derived from Akagi et al., 2011) by the ratio of O_3 to CO we estimated for that day. After five days,

304   we assumed no more O_3 was created, and we calculated the remaining amount of O_3 after day five using the box

305   model approach from Eq. (3). The concentration of O_3 on day five was C_o, and L was the lifetime of O_3 taken from

306   Myhre et al. (2013).

307   We converted the concentration of O_3 to Dobson units (DUs) and converted from DUs to radiative forcing

308 using a conversion factor from Myhre et al. (2013) each day after the fire. The radiative forcing in each year was

309 the mean radiative forcing of all the days within that year, although the annual forcing was negligible after the first

310 year.

311 **2.11 Ozone Precursors and Aerosols**

312   We used a method based on global warming potential (GWP), similar to Huang et al. (2016), to calculate

313 the radiative forcing of the ozone precursors and the direct aerosol effect. GWP is defined as the ratio of the time-

314 integrated radiative forcing of a pulse emission of a gaseous species to the time-integrated radiative forcing of an

315 equivalent emission mass of CO_2 (Joos et al., 2013). GWP is typically calculated for 20- and 100-year time

316 horizons. Here, we use GWPs to determine the warming effect of the precursor and aerosol emissions relative to

317 CH_4 at the 20- and 100-year time horizons, as shown in Eq. (8). We derive the radiative forcings for ozone

318 precursors and aerosols based on CH_4 because the radiative forcing of ozone precursors is through their effect on

319 methane over the long-term (Collins et al., 2013). Furthermore, the radiative forcing of CH_4 has the simplest

320 derivation in our model, so we assume it is the strongest continuous radiative forcing from which to build our

321 continuous model using GWP's.

322 $R_t = \frac{GWP_{t,x} \times EF_x}{GWP_{t,CH_4} \times EF_{CH_4}},$          (8)

323   The emissions factor (EF) and GWP are defined for gaseous species x, and the GWP is defined at the time

324 horizon t. For CO and NMVOCs, we interpolate this relative warming effect (R_t) between year one and year 20 by

325 assuming it remains constant. To interpolate this effect between years 20 and 100, we mirror the shape of methane's

326 cumulative radiative forcing curve over that time interval. From this curve we calculated the difference between

327 methane's cumulative radiative forcing at years 20 and 100. We then calculated the fractional decrease of this

328 difference each year between years 20 and 100. We multiplied those fractional decreases by the difference in R_t at

329 years 20 and 100 for CO and NMVOCs to derive a relative warming effect for the precursors. Finally, we

330 multiplied R_t by methane's cumulative radiative forcing curve to estimate the cumulative radiative forcing for each

331 precursor every year after the fire. We used the global GWPs for CO and NMVOCs from Myhre et al. (2013).

332   Since NO_x has a positive GWP at the 20-year time horizon and a negative GWP at the 100-year time

333 horizon, we chose not to mimic the shape of methane's radiative forcing curve when interpolating between the two

334 time points. Instead, we calculate an R_t value for NO_x at year one by scaling R_{20} in proportion to the change of

335   methane's cumulative radiative forcing from years one to 20. Then we interpolated between the R_t values in years

336   one, 20, and 100 using an exponential decay function of the form $ae^{-bx} + C$, whose coefficients were calculated

337   using the nls function in R (R Core Team 2020). We multiplied the R_t value for NO_x at each year by the cumulative

338   radiative forcing of CH_4 in that year to obtain a cumulative radiative forcing curve for NO_x. We use the global

339   GWP for NO_x from Myhre et al. (2013).

340   To calculate the cumulative radiative forcing from black and organic carbon direct effects, we used R_{20} and

341   multiplied this value by the cumulative radiative forcing curve of CH_4 in that year. These were summed to report

342   the aerosol radiative forcing together. Our calculations assume this entire cumulative radiative forcing happens in

343   the year of the fire, as fire aerosols are typically removed from the atmosphere via wet and dry deposition within a

344   matter of weeks (Bond et al., 2011, Quinn et al., 2008). We used the GWPs for black and organic carbon estimated

345   for open biomass burning including the cryosphere effect from Bond et al. (2011). To estimate the indirect aerosol

346   effect, we multiplied the radiative forcing of the direct effect of aerosols each year by the ratio of indirect to all sky

347   direct effect radiative forcing from wildfires defined in Ward et al. (2012).

348   **2.12 Statistical analyses**

349   All statistical analyses were completed in R (R Core Team 2020) using the nlme package (Pinheiro et al.,

350   2020). For the vegetative reference point heights, we created a linear fit model using the gls function with average

351   burn depth and height above the dense vegetation layer along the transect as the response variable in the burned and

352   unburned areas respectively. Both models were corrected for spatial autocorrelation between transect locations. We

353   chose the model with the lowest Akaike information criterion (AIC) score across five correlation structures,

354   exponential, Gaussian, linear, rational quadratic, and spherical to be our final model. In burned areas, the model had

355   vegetative reference point nested within burn severity type, while in unburned areas, we only modeled the effect of

356   vegetative reference point type. The model with the lowest AIC score for both burned and unburned areas had a

357   rational quadratic correlation structure.

358   To analyze differences in organic matter and carbon pools, height, and bulk density of the vegetation and

359   fibric soil layers we created linear mixed effect models using the lme function. These models had the soil or

360   vegetation layer characteristic value for each core as their response variable, vegetative reference point type as a

361   fixed effect, and transect number nested in site as random effects.

362   Finally, we created linear fit models using the gls function with organic matter combusted and carbon lost

363   at each transect in the burned areas as response variables with the same structure as the burn depth model. These

364   models had the lowest AIC scores with a rational quadratic correlation structure. An analysis of variance (ANOVA)

365   was used to test for significant differences between groups for all of our models.

366   **3 Results**

367   We found that burn depth measurements were consistent with burn severity classification, and burn depth

368   increased with fire severity (Fig. 3). Based on a two-factor ANOVA with vegetative reference point nested within

369   burn severity, differences in average transect burn depth were significant ($p < 0.0001$) between burn severity

370   categories. The ranges of moderate severity burn depth measurements overlapped substantially with the high and

371   low severity measurements. Moderate severity groups also had the most evenly distributed probability densities

372   across burn depth. *Dicranum* measurements captured the shallowest and the deepest burn depths (Fig. 3).

373   Nevertheless, across both vegetative reference points, there was a clear stepwise increase in burn depth across burn

374   severity classifications.
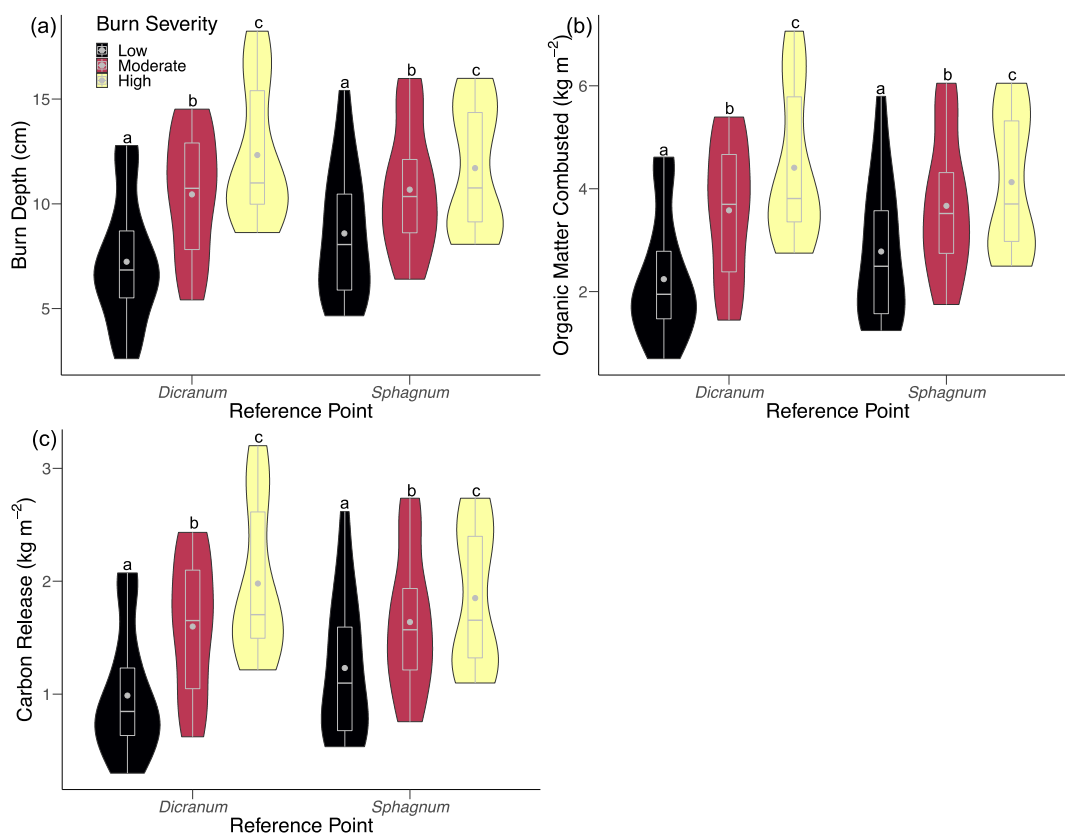
Figure 3. Distributions of average (a) burn depth, (b) organic matter combusted and (c) carbon released per unit
burned area per transect within each reference point across burn severity levels. Boxes encompass the middle 50%
of data, whiskers are the upper and lower quartiles, horizontal lines intersecting boxes show the median, and gray
points are the mean. Letters indicate significantly different groups of data.

We found no significant differences between vegetative reference point types in terms of mean organic

matter pool size, carbon pool size, height, or bulk density for either the live vegetation layer or fibric soil horizon

extracted in our unburned cores ($0.3504 < p < 0.9558$).

In the unburned areas, the fibric soil horizon (17.9 ± 0.63 cm) was nearly three times thicker than the

vegetation layer (6.19 ± 0.60 cm) to the depth that our cores reached (~30 cm; Table 1), which is likely an

underestimate of the soil organic layer depth, given that our cores only occasionally reached the mineral soil layer.

However, there was larger variation in the vegetation layer ($1\sigma = 6.9$ cm) than fibric horizon ($1\sigma = 2.6$ cm) height.

In most cases, the fire burned through the vegetation layer, but never completely through the fibric horizon (Fig. 3,

390   Table 1). The fibric layer (to 24.1 cm average) had almost three times greater organic matter and carbon pool sizes

391   compared to the vegetation layer because of its higher bulk density and height (Table 1).

392   **Table 1.** Bulk density, height, and carbon and organic matter percent and pool sizes of vegetation and fibric layers
393   measured in unburned soils averaged across reference points. Carbon and organic matter pool measurements are the
394   product of bulk density and their percent contents and are normalized to the height of the vegetation layer and 10
395   centimeters in the fibric layer. Sample size is 72, which is equally attributable to the two reference points. Error is
396   reported as SEM.

Layer	Bulk Density (kg m^{-3})	Height (cm)	Percent Carbon (%)	Carbon Pool (kg m^{-2})	Percent Organic Matter (%)	Organic Matter Pool (kg m^{-2})
Vegetation	26.7 ± 1.4	6.19 ± 0.60	43.04*	0.712 ± 0.037	100*	1.65 ± 0.09
Fibric	54.6 ± 5.0	17.9 ± 0.63	39.41 ± 0.56	2.07 ± 0.16	88.12 ± 1.17	4.48 ± 0.30

397   *Based on assumption
398
399   Carbon and dry organic matter loss estimates similarly increased with burn severity (Fig. 3, Table 2).

400   Based on a two-factor ANOVA with vegetative reference point nested in burn severity, average organic matter and

401   carbon loss differed between burn severity categories (carbon loss: $p < 0.0001$; organic matter loss: $p < 0.0001$) (Fig.

402   3). Similar to burn depth distributions, the moderate severity range overlapped with the high and low severity burn

403   distributions (Fig. 3).

404   **Table 2.** Carbon and organic matter loss averaged within each burn severity category across reference point, and
405   total carbon and organic mass loss over each burn severity category area. Total loss per burn severity category is
406   summed to calculate total loss over the total fire area by burn severity classification. Error is reported as SEM,
407   except for total loss over the fire area which is reported as the sum of errors.
408

Severity	Sample Size	Area (km^2)	Carbon Loss		Dry Organic Matter Loss	
			Average (kg m^{-2})	Total (Tg)	Average (kg m^{-2})	Total (Tg)
Low	36	130.01	1.11 ± 0.10	0.144 ± 0.013	2.51 ± 0.22	0.326 ± 0.029
Moderate	36	85.16	1.62 ± 0.10	0.138 ± 0.009	3.62 ± 0.22	0.309 ± 0.019
High	38	326.37	1.93 ± 0.12	0.629 ± 0.039	4.29 ± 0.23	1.40 ± 0.08
Total	158	541.54		0.911 ± 0.039 (Tg)		2.04 ± 0.09 (Tg)

409
410   The 2015 fires burned a total of 541.54 km^2 in the YKD. Most of the burned area (roughly 60%) was

411   classified as high severity, while moderate and low severity burns accounted for about 16% and 24%, respectively.

412   (Table 2). As a result, total organic matter and carbon loss within the high severity burn classification was over

413   three times greater than the other two burn severity categories. Although moderate severity occupied less fire area

414   than the low severity burn, it contained roughly equal total organic matter and carbon loss due to about 50% higher

415   organic matter and carbon losses per unit area on average. Summing carbon loss and dry organic matter loss over

416   the area of each burn severity category yielded a total loss of 2.04 ± 0.09 Tg of dry organic matter and 0.911 ± 0.039

417   Tg of carbon. This magnitude of total loss corresponded to an average 3.76 kg m^{-2} of organic matter and 1.68 kg m^{-2}

418   of carbon loss across the fire area.

419   The age of carbon increased by ~50 years from 5 to 20 cm in depth in the unburned area. Surface samples

420   from burned soils in a low severity area were dated to 2009, indicating a burn depth of about 5 cm or less, which is

421   within the range of our low severity burn depth measurements (Table 3). The rate of change in carbon age between

422   0 and 5 cm was 2.4 yr cm^{-1}; for the 15 to 20 cm interval it was 3.6 yr cm^{-1} . Because none of our burn depth

423   measurements exceeded 20 cm, all carbon released from the fire was relatively new carbon, younger than 64 years

424   of age. Our average burn depth of 10.3 cm across burn severity and reference point indicated an average age of

425   about 23 years for carbon released.

426 **Table 3.** The fraction of the modern standard and calibrated calendar age for each radiocarbon sample. Calendar
427 ages are the intercepts for the fraction modern value with the calibration curve. We do not consider the oldest
428 calendar ages.

Burn Status	Depth (cm)	Fraction Modern	Calendar Ages CE
Burned	0	1.0486 ± 0.0020	1957, 2009
Burned	0	1.0493 ± 0.0024	1957, 2009
Burned	0	1.0403 ± 0.0018	1957, 2008, 2009
Unburned	5	1.0625 ± 0.0020	1957, 2007, 2008, 2009
Unburned	10	1.1198 ± 0.0023	1958, 1996
Unburned	15	1.4603 ± 0.0024	1963, 1974
Unburned	20	1.0124 ± 0.0017	1956

429
430   The radiative forcing for gaseous and aerosol emissions from the 2015 fire season was positive for 80 years

431   post-fire according to our model, regardless of the future atmospheric gas concentration scenario (Fig. 4a).

432   However, the magnitude of the fire emissions' radiative forcings decreased with increasing ambient atmospheric gas

433   concentrations, with RCP 8.5 having the lowest radiative forcing at 80 years post-fire (Fig. 4a). Given the lack of

434   qualitative difference across future scenarios, below we present results for the RCP 4.5 scenario only (Table 4, Fig.

435   4b). Nitrogen oxides were the only gas with a negative radiative forcing at the 80-year cumulative mean. However,

436   they had a positive radiative forcing at the 20-year time horizon (Table 4). The only other negative radiative forcing

437   came from the indirect effect of aerosols that completely counterbalanced the positive radiative forcing from other

438   gaseous emissions in the first year, but the magnitude of this effect in terms of cumulative integrated forcing

439   diminished rapidly after the first decade (Fig. 4b). CO_2 produced the highest radiative forcing through 80 years

440   (Table 4, Fig. 4b). Nitrous oxide sustained its positive radiative forcing, however the radiative forcing was of

441   intermediate magnitude with respect to all gaseous emissions. In contrast, ozone and carbon monoxide exhibited

442   high radiative forcings, but the magnitude of these diminished rapidly with respect to carbon dioxide. Likewise, the

443   effect of the other ozone precursors, aerosols, and methane decreased relatively rapidly (Table 4). Overall, 20-years

444   post-fire, the effect of ozone precursors increased the total radiative forcing by roughly 11%. However, this percent

445   increase drops to 5% after 80 years, and the ozone precursors and aerosols show little effect on the percent reduction

446   of the total radiative forcing between 20- and 80-years post fire. Therefore, the positive radiative forcing is

447   sustained by long-lived gaseous emissions, especially carbon dioxide.
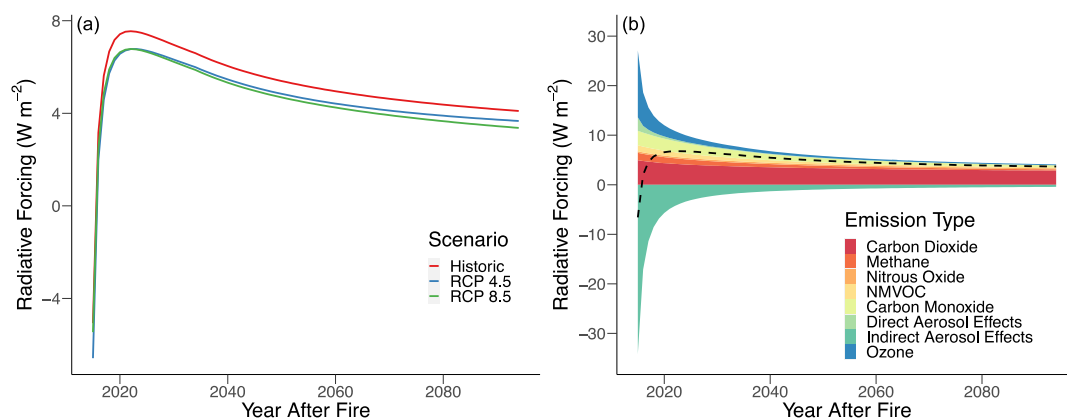
448
449   **Figure 4.** (a) Total cumulative mean radiative forcing of gaseous emissions for three future atmospheric gas
450   concentration scenarios, and (b) cumulative mean radiative forcing of different emissions (dashed line is net forcing)
451   under the RCP 4.5 future scenario over 80 years post-fire from the YKD 2015 fire season.

452
453   **Table 4.** Cumulative mean radiative forcing at 20- and 80- year time horizons post-fire for different greenhouse gas
454   and aerosol emissions from the 2015 fire season under the RCP 4.5 future scenario. Percent reduction refers to the
455   loss in radiative forcing when considering an 80-year time horizon compared to 20 years.

	Radiative Forcing (w m^{-2})										
Time Horizon	CO_2	CH_4	N_2O	O_3	NMVOC	CO	NO_x	Indirect Aerosol Effects	Direct Aerosol Effects	Total with Ozone Precursors and Aerosols	Total without Ozone Precursors and Aerosols
20 years	3.69	0.76	0.28	0.67	0.62	1.51	0.03	-1.71	0.14	5.99	5.41
80 years	2.87	0.24	0.22	0.17	0.19	0.40	-0.01	-0.43	0.03	3.67	3.49
Percent Reduction (%)	22	68	21	75	69	74	133	75	79	39	35

456
457   **4 Discussion**

458   Here we show that tundra wildfires release significant amounts of carbon and have a positive warming

459   effect on the atmosphere due to their gaseous and aerosol emissions over an 80-year time horizon, representing an

460   under-studied source of global greenhouse gasses under increasingly frequent tundra fire regimes. The 2015 fire

461   season in the YKD represents a large efflux of carbon from a wetland tundra ecosystem, generally not considered to

462   be highly vulnerable to fires. In total, we estimate that about 0.911 Tg of carbon was released from 541.54 km^2 of

463   burned area in the YKD, which, proportional to size, is roughly equivalent to the 2.1 Tg of carbon released from the

464   1,039 km^2 of burned area in the 2007 Anaktuvuk River fire reported by Mack et al. (2011). While the current status

465   of tundra ecosystems as a sink or source of carbon remains uncertain, the 2015 YKD fire season alone released

466   about a tenth of the carbon sequestered annually from tundra sink estimates (Virkkala et al., 2021). If tundra

467   ecosystems become a source of carbon to the atmosphere under warming, emissions from tundra wildfires may

468   further exacerbate this positive feedback to warming due to a changing balance between respiration and productivity

469   (Natali et al., 2019, Belshe et al., 2013). Note that we did not account for post-fire effects on net ecosystem

470   exchange of CO_2, which tend to be sources to the atmosphere with greater fire severity due to continued soil

471   respiration until sufficient vegetation recovers (Rocha and Shaver 2011a).

472   On average, both the tundra fires in the YKD and at Anaktuvuk River lost roughly 1.7 to 2.0 kg m^{-2} of

473   carbon (Mack et al., 2011). Carbon loss per area from tundra wildfires are within the range of total above- and

474   belowground carbon loss from boreal wildfires, approximately 0.5 to 4 kg m^{-2} (Walker et al., 2020a; Walker et al.,

475   2018b; Rogers et al., 2014), and close in value to the median wildfire loss of carbon, 2.54 kg m^{-2}, across all land

476   cover types in Alaska between 2001 and 2012 (Veraverbeke et al., 2015). Despite the additional combustion of

477   overstory vegetation in forests, carbon loss in both tundra and boreal systems comes primarily from belowground

478   organic matter (Walker et al., 2020a; Walker et al., 2018b; Rogers et al., 2014). While carbon loss per area of

479   tundra wildfire is similar to boreal wildfires, information on carbon emissions from tundra wildfires is substantially

480   more limited than boreal forest studies (He et al., 2021; Veraverbeke et al., 2021).

481   Given a fire return interval in the YKD of over around 200 years (Sae-Lim, 2019), fires there likely do not

482   burn through all the carbon accumulated since the last fire. However, tundra fires may initiate post-fire successional

483   trajectories, such as increased shrub cover, that may promote shorter fire return intervals (Hu et al., 2015; Rocha et

484   al., 2012). Shorter fire return intervals, in turn, gradually deplete the available soil carbon stocks. For example, He

485   et al. (2021) showed current tundra areas with frequent fire have relatively shallow soil organic layers. Moreover,

486   our radiocarbon data show that as fires burn deeper into the tundra, they release older carbon more rapidly because

487   the density of carbon by age increases. Coupling these burn-prone successional trajectories with projected increases

488   in tundra wildfire occurrence over the next century due to more frequent hot and dry conditions (Hu et al., 2015;

489   Rocha et al., 2012; Joly et al., 2012; Hu et al., 2010), as well as increases in lightning (Chen et al., 2021; Bieniek et

490   al., 2020; Veraverbeke et al., 2017), tundra wildfires may begin to burn carbon of an older age than the historic fire

491   return interval and hence transition some tundra regions into fire-driven carbon sources, similar to what has been

492   observed in North American boreal forests (Walker et al., 2019).

493   Immediate combustion is not the only impact wildfires have on tundra carbon stocks, nor do measures of

494   carbon loss fully describe the effect of wildfire emissions on the climate. Fires drive higher soil temperatures and

495   deeper active layer depths that can persist over multiple decades after fire (He et al., 2021; Hu et al., 2015; Rocha et

496   al., 2012), which is caused by the loss of insulating vegetation and upper soil layers from combustion (Rocha and

497   Shaver, 2011b). Higher soil temperatures and deeper active layer depths may catalyze permafrost degradation and

498   thermokarst development (Jones et al., 2015) that accelerates the effects of climate warming on tundra ecosystems.

499   Tundra fires also emit multiple gaseous and aerosol species, which have a net positive radiative forcing for at least

500   80 years post-fire. Hence, even if all of the carbon lost from fire in a tundra ecosystem were to be sequestered again

501   over time through increased photosynthesis, the long-term radiative impact of gaseous and aerosol emissions would

502   still generate atmospheric warming and thus positive climate feedbacks, which are amplified by post-fire permafrost

503   thaw and degradation and not accounted for in this study.

504   This positive radiative forcing is driven by sustained radiative forcings from long-lived greenhouse gasses

505   (GHGs), as well as significant contributions from short-lived climate forcers (SCLFs) such as ozone, NMVOCs, and

506   CO. Carbon dioxide has the highest radiative forcing at both short and long time horizons because it is emitted in

507   the highest quantity (Akagi et al., 2011) and its concentration decreases relatively slowly over time, especially in the

508   RCPs 4.5 and 8.5 scenarios (Joos et al., 2013). Aerosols and NO_x are SCLFs with both positive and negative

509   radiative forcings due to distinct mechanisms for affecting the Earth's radiative balance. Aerosols exert a direct

510   radiative forcing by reflecting or absorbing sunlight in the atmosphere and when deposited on high-albedo surfaces,

511   mainly snow and ice (Bond et al., 2011). Although black carbon aerosols have a positive and organic carbon

512   aerosols have a negative direct radiative forcing, the magnitude of black carbon's radiative forcing far exceeds that

513   from organic carbon (Myhre et al., 2013) (note these are combined in our representation). Indirectly, aerosols serve

514   as the nuclei for cloud formation, which increases the Earth's albedo and exerts a negative radiative forcing (Ward et

515   al., 2012). Nitrogen oxides have a near-term positive radiative forcing because they act in concert with NMVOCs

516   and CO to increase ozone concentrations, yet they have a long-term negative radiative forcing because they decrease

517   the lifetime of CH_4 (Collins et al., 2013).

518   We include a total radiative forcing with and without aerosols and ozone precursors, CO, NMVOCs, and

519   NO_x. The radiative forcing of these ozone precursors and aerosols is uncertain within current literature, especially

520   when originating in the Arctic, because of their short atmospheric lifetimes and dependence on regional transport

521   patterns (Bond et al., 2011, Quinn et al., 2008). However, the long-term cumulative radiative effect of these gaseous

522   emissions is relatively minimal in comparison to the long-lived GHGs and ozone, and both estimates of total

523   radiative forcing are of the same order of magnitude as previous estimates of the radiative forcing of gaseous

524   emissions from boreal forest fires (Huang et al., 2016; O'Halloran et al., 2012).

525   We found that as the predicted concentration of future emissions increases across RCP scenarios

526   (Meinshausen et al., 2011), the net radiative forcing of gaseous and aerosol emissions from tundra fires decreases

527   slightly. Although counterintuitive, this result is due to the dependency of the radiative forcing equations for long-

528   lived GHGs, namely CO_2, CH_4, and N_2O, on the ambient concentration of a gas. In more extreme future climate

529   scenarios, the atmosphere generally has higher concentrations of these GHGs, meaning the additional quantity of gas

530   emitted by the fire has a more diluted effect. This effect is largely counter-balanced by the fact that land and ocean

531   CO_2 sink capacities are diminished in more extreme future climate scenarios, leading to longer atmospheric CO_2

532   lifetimes (Fig. A7). The net result is that tundra wildfires have a relatively similar positive radiative forcing under

533   all future emissions scenarios.

534   Although wildfires in tundra ecosystems and boreal forests have similar positive radiative forcings through

535   their gaseous emissions, boreal forests also have significant multi decadal post-fire albedo changes due

536   predominantly to the combustion of overstory trees that expose snow in the fall, winter, and spring (Lyons et al.,

537   2008). Randerson et al. (2006) and O'Halloran et al. (2012) show that the negative radiative forcing of these albedo

538   changes can exceed the positive radiative forcing of gaseous emissions and generate a net cooling effect for boreal

539   forest fires over long time horizons in specific locations. It should be noted, however, that (i) the net cooling or

540   warming is heavily dependent on combustion levels, pre-fire canopy composition, and time horizon; (ii) fire-induced

541   albedo forcings predominantly impact the regional climate (Rogers et al., 2013), as opposed to globally-mixed

542   GHGs; and (iii) this cooling impact is expected to diminish with future climate change due to decreases in spring

543   snow cover (Potter et al., 2020).

544   In contrast, tundra ecosystems lack an overstory, and hence fires generate relatively short-lived decreases in

545   albedo (Rocha et al., 2012, French et al., 2016). These albedo changes are only caused by char and the exposed soil

546 surface in the summer because tundra vegetation rarely exists above the snow layer (Mack et al., 2011). As a result,

547 within four years after the Anaktuvuk River fire, low post-fire surface albedo recovered to its pre-fire reflectance as

548 the vegetation grew over the charred soil surface (French et al., 2016; Rocha and Shaver, 2011b). The decreased

549 surface reflectance contributes to increases in soil temperature and thaw depth after fire (Rocha and Shaver 2011b).

550 Therefore, the positive radiative forcing caused by tundra wildfire gaseous and aerosol emissions is not offset by

551 post-fire albedo changes as seen in boreal forest fires.

552   For the purpose of calculating the radiative forcing of wildfires in future research, we make our

553 computational code available on Github (see Code and Data Availability section). Our workflow is applicable to

554 wildfires in other arctic-boreal ecosystems, and could be applied to any ecosystem globally with the adjustment of

555 emissions factors of the specific material burning (Akagi et al., 2011) and global warming potentials for SCLFs

556 based on the geographic region of the wildfire (Myhre et al., 2013). As a result, our method of calculating the

557 radiative forcing of wildfires can be used for studies across multiple regions with the appropriate parameters, which

558 can advance a more complete understanding of the effects of wildfires on the climate.

559   Future work could clarify some of the uncertainties that were not explicitly analyzed in our final estimates

560 of carbon loss and radiative forcing. Regarding our estimates of carbon loss from the YKD fires, we did not account

561 for combustion of aboveground tall woody vegetation, predominantly confined to peat plateau edges. Although this

562 biomass was sparse on the tundra landscape, it represents an additional source of carbon from combustion (for

563 boreal forest fires, see Walker et al., 2020c). Despite the lack of difference we found between soil and vegetation

564 matter characteristics across vegetative reference point groups, there could have been variation in these

565 characteristics outside of the primarily peat plateau areas that we sampled. Furthermore, the fact that *Dicranum*

566 accounted for a larger range of burn depths, though not significantly different from *Sphagnum*, could indicate more

567 variable burn dynamics around *Dicranum* or better efficacy of *Dicranum* for measuring extreme burn depths, which

568 highlights the potential bias introduced by choosing specific combustion markers. Likewise, we eliminated tussock

569 measurements from our final analysis because they were relatively scarce on the landscape and yielded inconsistent

570 results, perhaps due to burn dynamics around tussocks that remain obscure using our combustion measurement

571 method. Another robust analysis of carbon loss would seek to minimize potential bias and find combustion markers

572 and soil characteristics for different land cover types at a higher resolution within a fire, similar to how different

573 combustion markers are used regionally (Walker et al., 2020c; Mack et al., 2011; Boby et al., 2010).

574   Regarding spatial scaling of fire emissions, our assignment of low, moderate, and high severity was based

575 on our particular collection of field measurements and therefore may not translate well to other fire complexes. We

576 also used a relatively simple method for extrapolating emissions based on fire severity. More involved techniques

577 such as relating mechanism-based geospatial predictors to field plots using statistical techniques and machine

578 learning, which has been employed for boreal forests in Alaska and Canada (Dieleman et al., 2020; Walker et al.,

579 2018b; Veraverbeke et al., 2015; Rogers et al., 2014), would likely yield more robust estimates for regional

580 emissions. In this context, we strongly recommend increasing the number of tundra fire carbon emission

581 observations in different regions to facilitate synthesis and biome-wide modeling, as has been done for boreal forests

582 (Walker et al., 2020a,b,c).

583   Our radiative forcings model uses data and algorithms from multiple previous studies, including for

584 emissions factors (Akagi et al., 2011), RCP scenarios (Meinshausen et al,. 2011), GWPs (Myhre et al., 2013), ozone

585 and CO concentration ratios (Jaffe and Widger, 2012), and aerosol direct and indirect effects (Ward et al., 2012), all

586 of which may not be geographically, biologically, or temporally specific to the YKD fires. These factors are also

587 known to be variable depending on fuel types, fire severity and lifetime, and atmospheric dynamics at the time of

588 and following fire (e.g., Wiggins et al., 2016; Jaffe and Widger, 2012; Chen et al., 2009). Furthermore, our model

589 does not include the potential mitigating or exacerbating effects of post-fire ecosystem changes on gas

590 concentrations, such as changes in post-fire vegetation (Frost et al., 2020; Zhou et al., 2019; Barrett et al., 2012),

591 increased soil respiration (Rocha and Shaver, 2011a), and increased active layer depths and permafrost degradation

592 (Holloway et al., 2020; Jafarov et al., 2013; Rocha et al., 2012). With reparameterizations specific to individual

593 fires, our model could be made more accurate for future work.

594 **5 Conclusions**

595   To our knowledge, our study is the first to account for both carbon loss and radiative forcing from tundra

596 wildfires. We develop a method that pairs *in situ* measurements of combustion levels from local pre-fire reference

597 points with remotely sensed burn severity data to scale organic matter and carbon loss to the entire fire area. Our

598 estimate of the radiative forcing of gaseous and aerosol emissions from the fire event suggests that tundra wildfires

599 positively reinforce climate warming; however, the role of post-fire vegetative regeneration in mitigating these

600 carbon emissions remains unknown. Our results stress the importance of considering tundra wildfires in assessing

601 climate feedbacks and the need for future research that more explicitly discerns the warming effect of fires across

602 the tundra biome.

603

604

605

606

607

608

609

610

611

612

613

614

615

616

617

618

619

620

621

622

623

624

625

626

627

628

629   **Appendix A**
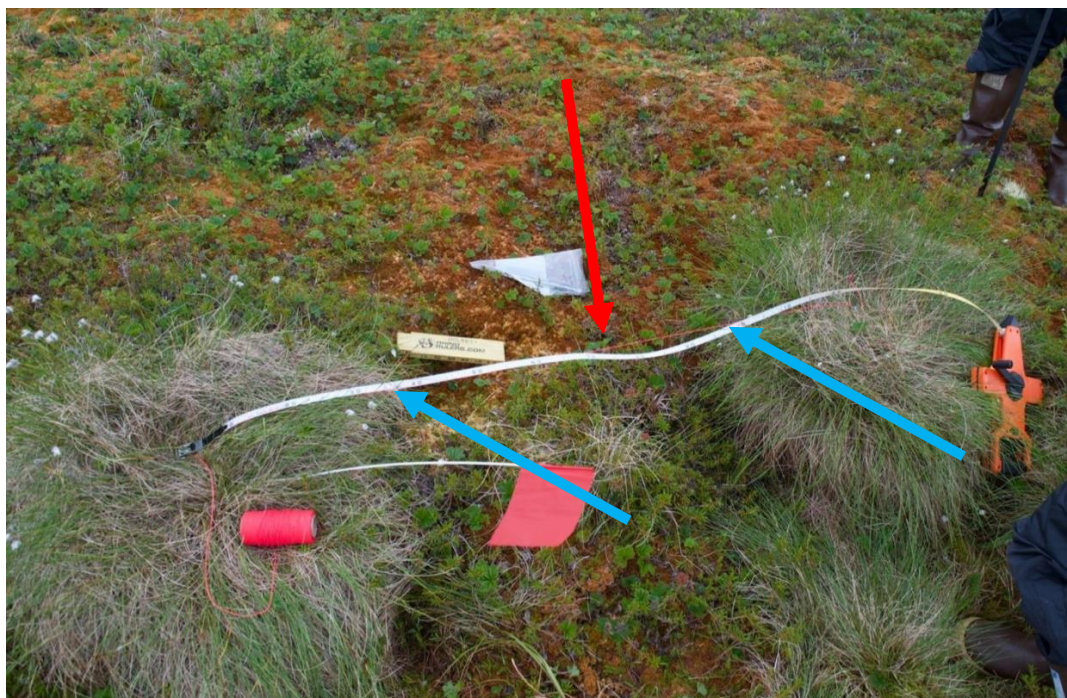
630
631   **Figure A1.** Height measurement of *Eriophorum vaginatum* in an unburned area from the taut string (red arrow) to
632   the dense vegetation layer between the starting and ending points (blue arrows) at the edge of each tussock patch.
633
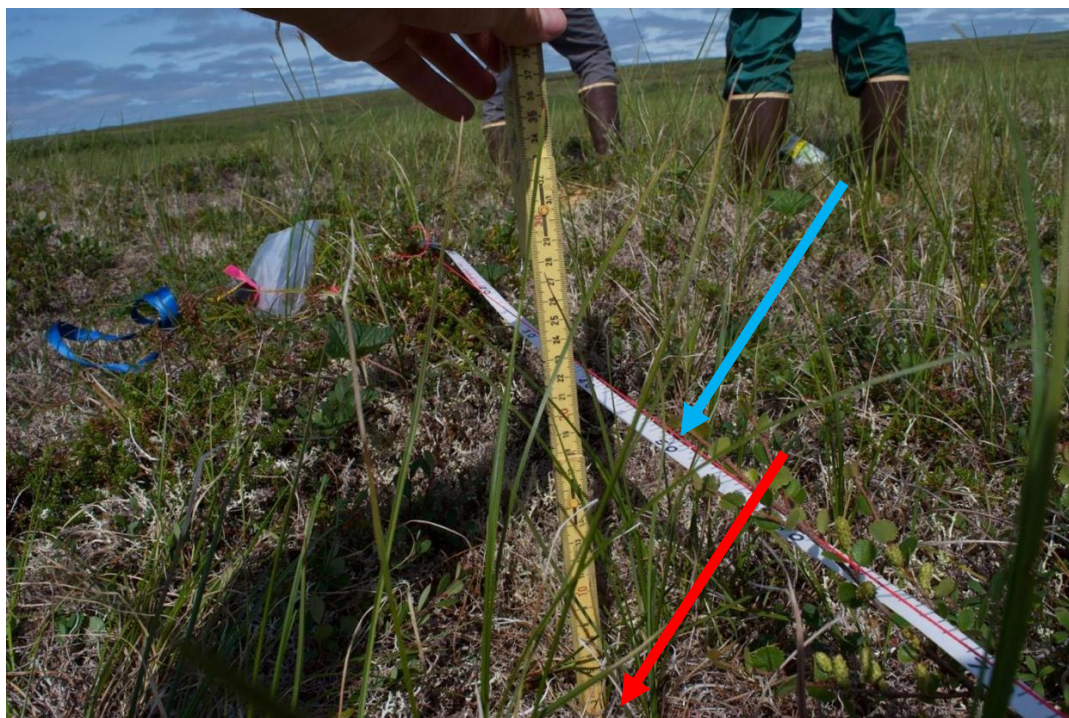
634
635 **Figure A2.** Measurement from the taut string to the dense vegetative layer (red arrow) in an unburned area every 25
636 centimeters (blue arrow).
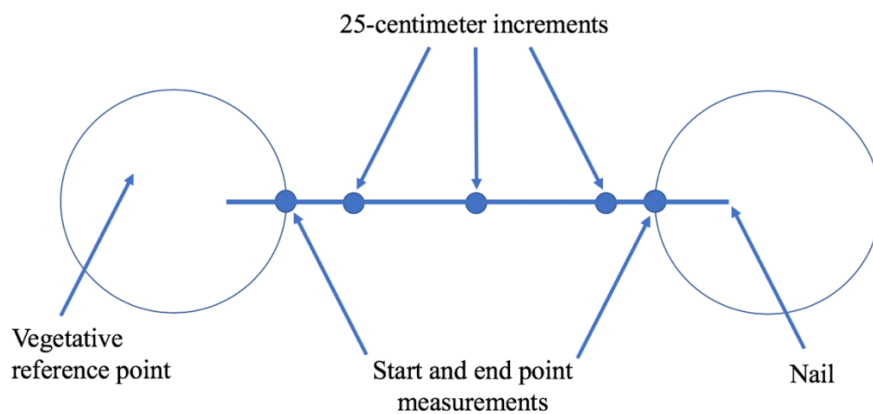
637
638 **Figure A3.** A schematic of the height measurements made along a transect between two vegetative reference points.
639
640
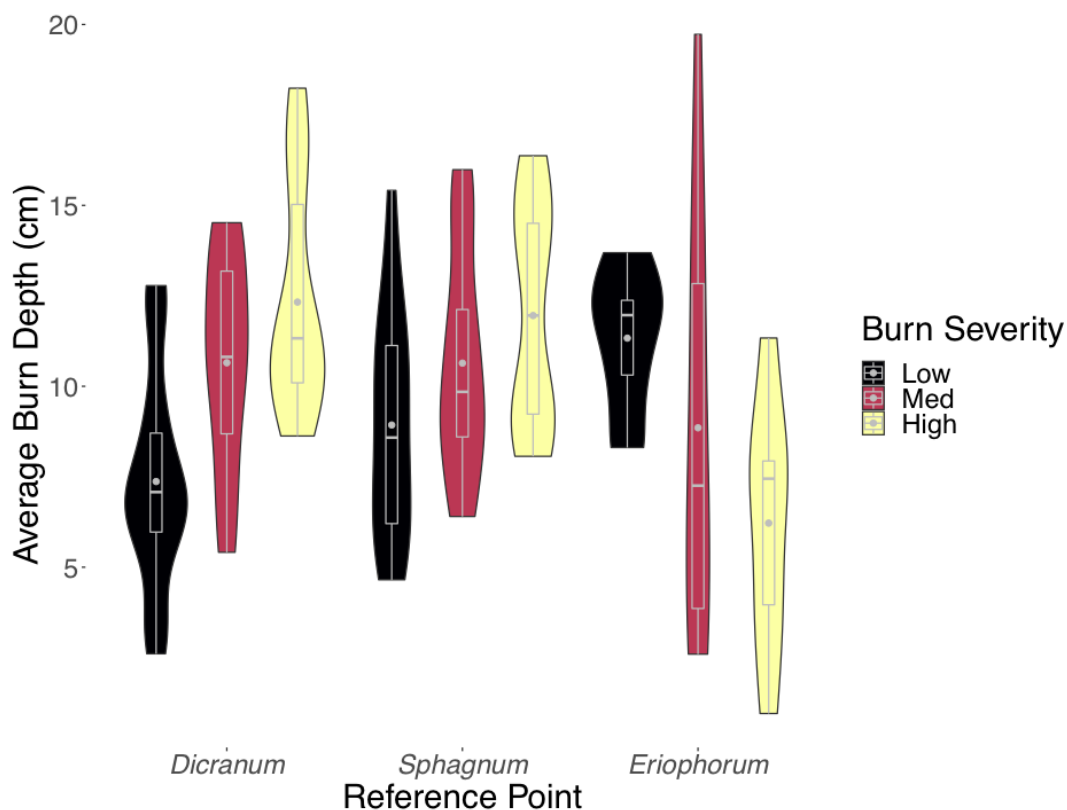
641
642 **Figure A4.** The distributions of average burn depth per transect within each reference point (including *Eriophorum*
643 *vaginatum*) across burn severity. Boxes encompass the middle 50% of data, whiskers are the upper and lower
644 quartiles, horizontal lines intersecting boxes show the median, and gray points are the mean.
645
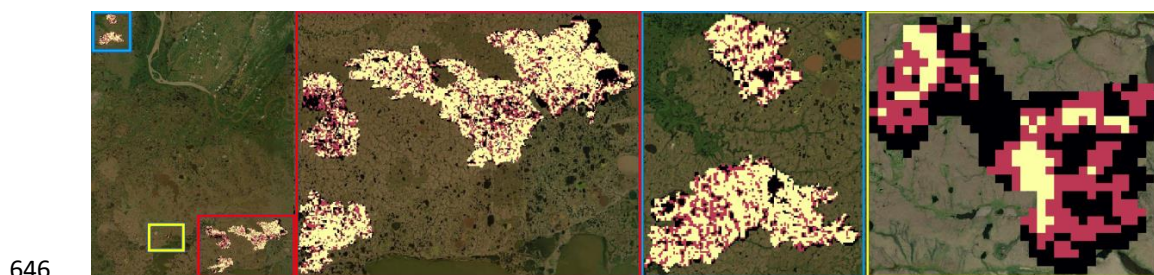
646

647 **Figure A5.** Fire severity across the YKD 2015 fire area categorized using dNBR values into low (black), moderate
648 (red), and high (yellow) severity categories. The panels show the total fire area (far left), then close ups of the
649 southeastern (red), northwestern (blue), and south-central (yellow) fire scars, respectively. Basemap sources: Esri,
650 DigitalGlobe, GeoEye, i-cubed, USDA FSA, USGS, AEX, Getmapping, Aerogrid, IGN, IGP, swisstopo, and the
651 GIS User Community.
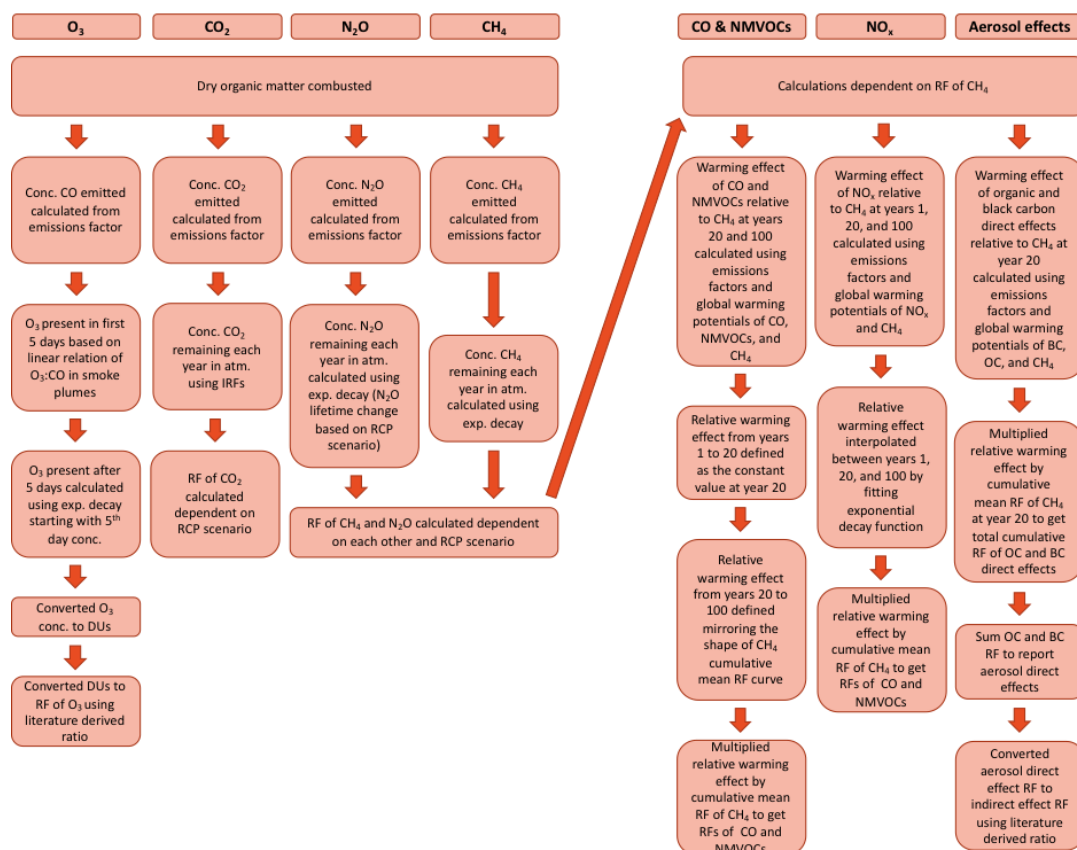
Figure A6. Flowchart of the methodology for the calculation of the radiative forcings of gaseous emissions from biomass combustion generally applicable to any biome with adjustment of biome-specific parameters.

652
653
654
655
656
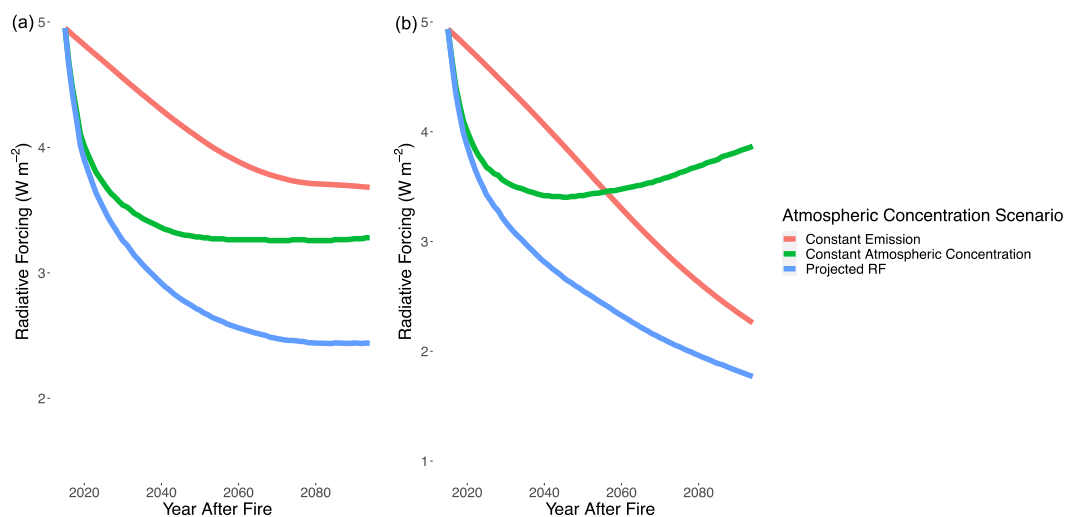
657
658
659 **Figure A7.** The radiative forcing of CO_2 emitted from the 2015 YKD fire season for RCP 4.5 (a) and 8.5 (b) when
660 (i) holding the emission constant (red lines) so that no emitted CO_2 is sequestered, (ii) holding the background
661 atmospheric concentration constant (green lines), and (iii) the combination of these, resulting in our main CO_2
662 radiative forcing equation (blue lines; Eq. 7). In the case of (i, red lines), increasing atmospheric CO_2 concentrations
663 dampen the radiative impact of fire-emitted CO_2. In the case of (ii, green lines), the only time-varying impact on
664 CO_2 radiative forcing is ocean and land sinks, which become less effective and even reverse with more extreme
665 climate change according to model results presented in Joos et al. (2013). These lines are similar to the impulse
666 response function of CO_2 for their respective scenarios in Joos et al. (2013).
667

668 **Code and Data Availability**

669 The radiative forcings calculation code is available on GitHub and Zenodo via DOI: 10.5281/zenodo.6617455

670 (Moubarak, 2022). All field and lab raw data used in this study, including vegetative reference point height

671 measurements and soil and vegetation core metrics, and combustion data products derived from our calculations are

672 publicly available in the NSF Arctic Data Center via DOI:10.18739/A2PR7MV5P (Moubarak et al., 2020).

673 **Author Contributions**

674 MM, BR, SS, and SN were involved with conceptualization, funding acquisition, and methodology. SP completed

675 investigation of burn severity data and jointly completed visualization with MM. MM, SS, and BR did investigation

676 of burn depth measurements and soil and vegetation characteristics. MM analyzed data and developed the radiative

677 forcings model. SS and SN did project administration for the field sampling. MM curated data and wrote the

678 original manuscript draft. MM, BR, SS, SP, and SN reviewed and edited the final published work.

679 **Competing Interests**

680 The authors declare that they have no conflict of interest.

Acknowledgements

This work was funded by the National Science Foundation (NSF-1915307 to SMN, NSF-1915307 to SS), Casstevens Family Fund (to MM), and the National Aeronautics and Space Administration (NASA) Arctic-Boreal Vulnerability Experiment (ABoVE; NNX15AU56A to BR) and the Gordon and Betty Moore Foundation (8414 to SMN and BR). The authors would like to thank Dr. William Pfitsch for his helpful mentorship in the synthesis of this project and creation of the written work. Also, the authors would like to thank Dr. Catherine Beck for offering her knowledge about radiocarbon sample preparation and analysis.

References

Akagi, S. K., Yokelson, R. J., Wiedinmyer, C., Alvarado, M. J., Reid, J. S., Karl, T., Crounse, J. D. and Wennberg, P. O.: Emission factors for open and domestic biomass burning for use in atmospheric models, Atmospheric Chemistry and Physics, 11, 4039-4072, https://doi.org/10.5194/acp-11-4039-2011, 2011.

Barrett, K., Rocha, A. V., van de Weg, Martine Janet and Shaver, G.: Vegetation shifts observed in arctic tundra 17 years after fire, Remote Sensing Letters, 3, 729-736, https://doi.org/10.1080/2150704X.2012.676741, 2012.

Belshe, E. F., Schuur, E. and Bolker, B. M.: Tundra ecosystems observed to be CO2 sources due to differential amplification of the carbon cycle, Ecol. Lett., 16, 1307-1315, https://doi.org/10.1111/ele.12164, 2013.

Bieniek, P. A., Bhatt, U. S., York, A., Walsh, J. E., Lader, R., Strader, H., Ziel, R., Jandt, R. R. and Thoman, R. L.: Lightning variability in dynamically downscaled simulations of Alaska's present and future summer climate, Journal of Applied Meteorology and Climatology, 59, 1139-1152, https://doi.org/10.1175/JAMC-D-19-0209.1, 2020.

Boby, L. A., Schuur, E. A., Mack, M. C., Verbyla, D. and Johnstone, J. F.: Quantifying fire severity, carbon, and nitrogen emissions in Alaska's boreal forest, Ecol. Appl., 20, 1633-1647, https://doi.org/10.1890/08-2295.1, 2010.

Bond, T. C., Zarzycki, C., Flanner, M. G. and Koch, D. M.: Quantifying immediate radiative forcing by black carbon and organic matter with the Specific Forcing Pulse, Atmospheric Chemistry and Physics, 11, 1505-1525, https://doi.org/10.5194/acp-11-1505-2011, 2011.

Chen, Y., Li, Q., Randerson, J. T., Lyons, E. A., Kahn, R. A., Nelson, D. L. and Diner, D. J.: The sensitivity of CO and aerosol transport to the temporal and vertical distribution of North American boreal fire emissions, Atmospheric Chemistry and Physics, 9, 6559-6580, https://doi.org/10.5194/acp-9-6559-2009, 2009.

Chen, Y., Romps, D. M., Seeley, J. T., Veraverbeke, S., Riley, W. J., Mekonnen, Z. A. and Randerson, J. T.: Future increases in Arctic lightning and fire risk for permafrost carbon, Nature Climate Change, 11, 404-410, https://doi.org/10.1038/s41558-021-01011-y, 2021.

Cohen, J., Zhang, X., Francis, J., Jung, T., Kwok, R., Overland, J., Ballinger, T., Blackport, R., Bhatt, U. S. and Chen, H.: Arctic change and possible influence on mid-latitude climate and weather: a US CLIVAR White Paper, US CLIVAR reports, https://doi.org/10.5065/D6TH8KGW, 2018.

Collins, W. J., Fry, M. M., Yu, H., Fuglestvedt, J. S., Shindell, D. T. and West, J. J.: Global and regional temperature-change potentials for near-term climate forcers, Atmospheric Chemistry and Physics, 13, 2471-2485, https://doi.org/10.5194/acp-13-2471-2013, 2013.

Dieleman, C. M., Rogers, B. M., Potter, S., Veraverbeke, S., Johnstone, J. F., Laflamme, J., Solvik, K., Walker, X. J., Mack, M. C. and Turetsky, M. R.: Wildfire combustion and carbon stocks in the southern Canadian boreal forest: Implications for a warming world, Global Change Biol., 26, 6062-6079, https://doi.org/10.1111/gcb.15158, 2020.

719 French, N. H., Whitley, M. A. and Jenkins, L. K.: Fire disturbance effects on land surface albedo in Alaskan tundra,
720 Journal of Geophysical Research: Biogeosciences, 121, 841-854, https://doi.org/10.1002/2015JG003177, 2016.
721

722 Frost, G. V., Loehman, R. A., Saperstein, L. B., Macander, M. J., Nelson, P. R., Paradis, D. P. and Natali, S. M.:
723 Multi-decadal patterns of vegetation succession after tundra fire on the Yukon-Kuskokwim Delta, Alaska,
724 Environmental Research Letters, 15, 025003, https://doi.org/10.1088/1748-9326/ab5f49, 2020.

725 Gorelick, N., Hancher, M., Dixon, M., Ilyushchenko, S., Thau, D. and Moore, R.: Google Earth Engine: Planetary-
726 scale geospatial analysis for everyone, Remote Sens. Environ., 202, 18-27, https://doi.org/10.1016/j.rse.2017.06.031,
727 2017.

728 He, J., Chen, D., Jenkins, L. and Loboda, T. V.: Impacts of wildfire and landscape factors on organic soil properties
729 in Arctic tussock tundra, Environmental Research Letters, 16, 085004, https://doi.org/10.1088/1748-9326/ac1192,
730 2021.

731 Holloway, J. E., Lewkowicz, A. G., Douglas, T. A., Li, X., Turetsky, M. R., Baltzer, J. L. and Jin, H.: Impact of
732 wildfire on permafrost landscapes: A review of recent advances and future prospects, Permafrost Periglacial
733 Processes, 31, 371-382, https://doi.org/10.1002/ppp.2048, 2020.

734 Hu, F. S., Higuera, P. E., Duffy, P., Chipman, M. L., Rocha, A. V., Young, A. M., Kelly, R. and Dietze, M. C.:
735 Arctic tundra fires: natural variability and responses to climate change, Frontiers in Ecology and the Environment,
736 13, 369-377, https://doi.org/10.1890/150063, 2015.

737 Hu, F. S., Higuera, P. E., Walsh, J. E., Chapman, W. L., Duffy, P. A., Brubaker, L. B. and Chipman, M. L.: Tundra
738 burning in Alaska: linkages to climatic change and sea ice retreat, Journal of Geophysical Research: Biogeosciences,
739 115, https://doi.org/10.1029/2009JG001270, 2010.

740 Hua, Q., Barbetti, M. and Rakowski, A. Z.: Atmospheric radiocarbon for the period 1950–2010, Radiocarbon, 55,
741 2059-2072, https://doi.org/10.2458/azu_js_rc.v55i2.16177, 2013.

742 Huang, S., Liu, H., Dahal, D., Jin, S., Li, S. and Liu, S.: Spatial variations in immediate greenhouse gases and
743 aerosol emissions and resulting radiative forcing from wildfires in interior Alaska, Theoretical and applied
744 climatology, 123, 581-592, https://doi.org/10.1007/s00704-015-1379-0, 2016.

745 IPCC: Climate Change 2021: The Physical Science Basis, Contribution of Working Group I to the Sixth Assessment
746 Report of the Intergovernmental Panel on Climate Change, edited by: Masson-Delmotte, V., Zhai, P., Pirani, A.,
747 Connors, S.L., Péan, C., Berger, S., Caud, N., Chen, Y., Goldfarb, L., Gomis, M.I., Huang, M., Leitzell, K., Lonnoy,
748 E., Matthews, J.B.R., Maycock, T.K., Waterfield, T., Yelekçi, O., Yu, R. and Zhou, B., Cambridge University Press,
749 Cambridge, United Kingdom and New York, NY, USA, In press, https://doi.org/10.1017/9781009157896, 2021.
750

751 Jafarov, E. E., Romanovsky, V. E., Genet, H., McGuire, A. D. and Marchenko, S. S.: The effects of fire on the
752 thermal stability of permafrost in lowland and upland black spruce forests of interior Alaska in a changing climate,
753 Environmental Research Letters, 8, 035030, https://doi.org/10.1088/1748-9326/8/3/035030, 2013.

754 Jaffe, D. A. and Wigder, N. L.: Ozone production from wildfires: A critical review, Atmos. Environ., 51, 1-10,
755 https://doi.org/10.1016/j.atmosenv.2011.11.063, 2012.

756 Joly, K., Duffy, P. A. and Rupp, T. S.: Simulating the effects of climate change on fire regimes in Arctic biomes:
757 implications for caribou and moose habitat, Ecosphere, 3, 1-18, https://doi.org/10.1890/ES12-00012.1, 2012.
758

759 Jones, B. M., Grosse, G., Arp, C. D., Miller, E., Liu, L., Hayes, D. J. and Larsen, C. F.: Recent Arctic tundra fire
760 initiates widespread thermokarst development, Scientific reports, 5, 1-13, https://doi.org/10.1038/srep15865, 2015.
761

762 Joos, F., Roth, R., Fuglestvedt, J. S., Peters, G. P., Enting, I. G., Bloh, W. v., Brovkin, V., Burke, E. J., Eby, M. and
763 Edwards, N. R.: Carbon dioxide and climate impulse response functions for the computation of greenhouse gas
764 metrics: a multi-model analysis, Atmospheric Chemistry and Physics, 13, 2793-2825, https://doi.org/10.5194/acp-
765 13-2793-2013, 2013.

766 Jorgenson, M. T.: Hierarchical organization of ecosystems at multiple spatial scales on the Yukon-Kuskokwim
767 Delta, Alaska, USA, Arct. Antarct. Alp. Res., 32, 221-239, https://doi.org/10.1080/15230430.2000.12003360, 2000.

768 Key, C. H. and Benson, N. C.: Landscape assessment (LA), In: Lutes, Duncan C.; Keane, Robert E.; Caratti, John
769 F.; Key, Carl H.; Benson, Nathan C.; Sutherland, Steve; Gangi, Larry J.2006.FIREMON: Fire effects monitoring
770 and inventory system. Gen. Tech. Rep. RMRS-GTR-164-CD. Fort Collins, CO: US Department of Agriculture,
771 Forest Service, Rocky Mountain Research Station.p.LA-1-55, 164, https://www.fs.usda.gov/treesearch/pubs/24066,
772 2006.

773 Kimball, J. S., Zhao, M., McDonald, K. C. and Running, S. W.: Satellite remote sensing of terrestrial net primary
774 production for the pan-Arctic basin and Alaska, Mitigation Adapt. Strat. Global Change, 11, 783-804,
775 https://doi.org/10.1007/s11027-005-9014-5, 2006.

776 Lindgren, A., Hugelius, G. and Kuhry, P.: Extensive loss of past permafrost carbon but a net accumulation into
777 present-day soils, Nature, 560, 219-222, https://doi.org/10.1038/s41586-018-0371-0, 2018.

778 Lyons, E. A., Jin, Y. and Randerson, J. T.: Changes in surface albedo after fire in boreal forest ecosystems of
779 interior Alaska assessed using MODIS satellite observations, Journal of Geophysical Research: Biogeosciences,
780 113, https://doi.org/10.1029/2007JG000606, 2008.

781 Ma, S., He, F., Tian, D., Zou, D., Yan, Z., Yang, Y., Zhou, T., Huang, K., Shen, H. and Fang, J.: Variations and
782 determinants of carbon content in plants: a global synthesis, Biogeosciences, 15, 693-702,
783 https://doi.org/10.5194/bg-15-693-2018, 2018.

784 Mack, M. C., Bret-Harte, M. S., Hollingsworth, T. N., Jandt, R. R., Schuur, E. A., Shaver, G. R. and Verbyla, D. L.:
785 Carbon loss from an unprecedented Arctic tundra wildfire, Nature, 475, 489-492,
786 https://doi.org/10.1038/nature10283, 2011.

787 Meinshausen, M., Smith, S. J., Calvin, K., Daniel, J. S., Kainuma, M. L., Lamarque, J., Matsumoto, K., Montzka, S.
788 A., Raper, S. C. and Riahi, K.: The RCP greenhouse gas concentrations and their extensions from 1765 to 2300,
789 Clim. Change, 109, 213-241, https://doi.org/10.1007/s10584-011-0156-z, 2011.

790 Moubarak, M.: Radiative forcings of gaseous emissions, Zenodo [code], https://doi.org/10.5281/zenodo.6617455,
791 2022.

792 Moubarak, M., Sistla, S. and Natali, S. M.: Yukon-Kuskokwim River Delta 2015 fire burn depth measurements and
793 unburned soil and vegetation organic matter and carbon content collected in 2019, Arctic Data Center [data set],
794 https://doi.org/10.18739/A2DN3ZX3Q, 2020.

795 Myhre, G., Highwood, E. J., Shine, K. P. and Stordal, F.: New estimates of radiative forcing due to well mixed
796 greenhouse gases, Geophys. Res. Lett., 25, 2715-2718, https://doi.org/10.1029/98GL01908, 1998.

797 Myhre, G., Shindell, D., Bréon, F.-M., Collins, W., Fuglestvedt, J., Huang, J., Koch, D., Lamarque, J.-F., Lee, D.,
798 Mendoza, B., Nakajima, T., Robock, A., Stephens, G., Takemura, T., and Zhang, H.: Anthropogenic and Natural
799 Radiative Forcing, in: Climate Change: The Physical Science Basis. Contribution of Working Group I to the Fifth
800 Assessment Report of the Intergovernmental Panel on Climate Change, edited by: Stocker, T.F., Qin, D., Plattner,
801 G.-K., Tignor, M., Allen, S.K., Boschung, J., Nauels, A., Xia, Y., Bex, V. and Midgley, P.M., Cambridge University
802 Press, Cambridge, United Kingdom and New York, NY, USA, 659–740, https://doi.org/10.1017/
803 CBO9781107415324.018, 2013.
804
805 Natali, S. M., Schuur, E. A., Mauritz, M., Schade, J. D., Celis, G., Crummer, K. G., Johnston, C., Krapek, J.,
806 Pegoraro, E. and Salmon, V. G.: Permafrost thaw and soil moisture driving CO2 and CH4 release from upland
807 tundra, Journal of Geophysical Research: Biogeosciences, 120, 525-537, https://doi.org/10.1002/2014JG002872,
808 2015.

809 Natali, S. M., Watts, J. D., Rogers, B. M., Potter, S., Ludwig, S. M., Selbmann, A., Sullivan, P. F., Abbott, B. W.,
810 Arndt, K. A. and Birch, L.: Large loss of CO 2 in winter observed across the northern permafrost region, Nature
811 Climate Change, 9, 852-857, https://doi.org/10.1038/s41558-019-0592-8, 2019.

O'Halloran, T. L., Law, B. E., Goulden, M. L., Wang, Z., Barr, J. G., Schaaf, C., Brown, M., Fuentes, J. D., Göckede, M. and Black, A.: Radiative forcing of natural forest disturbances, Global Change Biol., 18, 555-565, https://doi.org/10.1111/j.1365-2486.2011.02577.x, 2012.

Pinheiro J, Bates D, DebRoy S, Sarkar D, and R Core Team: nlme: Linear and Nonlinear Mixed Effects Models, R package version 3.1-149, https://CRAN.R-project.org/package=nlme, 2020.

Potter, S., Solvik, K., Erb, A., Goetz, S. J., Johnstone, J. F., Mack, M. C., Randerson, J. T., Román, M. O., Schaaf, C. L. and Turetsky, M. R.: Climate change decreases the cooling effect from postfire albedo in boreal North America, Global Change Biol., 26, 1592-1607, https://doi.org/10.1111/gcb.14888, 2020.

Quinn, P. K., Bates, T. S., Baum, E., Doubleday, N., Fiore, A. M., Flanner, M., Fridlind, A., Garrett, T. J., Koch, D. and Menon, S.: Short-lived pollutants in the Arctic: their climate impact and possible mitigation strategies, Atmospheric Chemistry and Physics, 8, 1723-1735, https://doi.org/10.5194/acp-8-1723-2008, 2008.

R Core Team: R: A language and environment for statistical computing, R Foundation for Statistical Computing, Vienna, Austria, https://www.R-project.org/, 2020.

Ramsey, C. B.: Bayesian analysis of radiocarbon dates, Radiocarbon, 51, 337-360, https://doi.org/10.1017/S0033822200033865, 2009.

Randerson, J. T., Liu, H., Flanner, M. G., Chambers, S. D., Jin, Y., Hess, P. G., Pfister, G., Mack, M. C., Treseder, K. K. and Welp, L. R.: The impact of boreal forest fire on climate warming, Science, 314, 1130-1132, https://doi.org/10.1126/science.1132075, 2006.

Raynolds, M. K., Walker, D. A. and Maier, H. A.: Plant community-level mapping of arctic Alaska based on the Circumpolar Arctic Vegetation Map, Phytocoenologia, 35, 821, https://doi.org/10.1127/0340-269X/2005/0035-0821, 2005.

Reimer, P. J., Brown, T. A. and Reimer, R. W.: Discussion: reporting and calibration of post-bomb 14C data, Radiocarbon, 46, 1299-1304, https://doi.org/10.1017/S0033822200033154, 2004.

Rocha, A. V., Loranty, M. M., Higuera, P. E., Mack, M. C., Hu, F. S., Jones, B. M., Breen, A. L., Rastetter, E. B., Goetz, S. J. and Shaver, G. R.: The footprint of Alaskan tundra fires during the past half-century: implications for surface properties and radiative forcing, Environmental Research Letters, 7, 044039, https://doi.org/10.1088/1748-9326/7/4/044039, 2012.

Rocha, A. V. and Shaver, G. R.: Burn severity influences postfire CO2 exchange in arctic tundra, Ecol. Appl., 21, 477-489, https://doi.org/10.1890/10-0255.1, 2011a.

Rocha, A. V. and Shaver, G. R.: Postfire energy exchange in arctic tundra: the importance and climatic implications of burn severity, Global Change Biol., 17, 2831-2841, https://doi.org/10.1111/j.1365-2486.2011.02441.x, 2011b.

Rogers, B. M., Randerson, J. T. and Bonan, G. B.: High-latitude cooling associated with landscape changes from North American boreal forest fires, Biogeosciences, 10, 699-718, https://doi.org/10.5194/bg-10-699-2013, 2013.

Rogers, B. M., Veraverbeke, S., Azzari, G., Czimczik, C. I., Holden, S. R., Mouteva, G. O., Sedano, F., Treseder, K. K. and Randerson, J. T.: Quantifying fire-wide carbon emissions in interior Alaska using field measurements and Landsat imagery, Journal of Geophysical Research: Biogeosciences, 119, 1608-1629, https://doi.org/10.1002/2014JG002657, 2014.

Sae-Lim, J., Russell, J. M., Vachula, R. S., Holmes, R. M., Mann, P. J., Schade, J. D. and Natali, S. M.: Temperature-controlled tundra fire severity and frequency during the last millennium in the Yukon-Kuskokwim Delta, Alaska, The Holocene, 29, 1223-1233, https://doi.org/10.1177/0959683619838036, 2019.

Schuur, E. A., McGuire, A. D., Schädel, C., Grosse, G., Harden, J. W., Hayes, D. J., Hugelius, G., Koven, C. D., Kuhry, P. and Lawrence, D. M.: Climate change and the permafrost carbon feedback, Nature, 520, 171-179, https://doi.org/10.1038/nature14338, 2015.

857 Shaw, R. D.: An archaeology of the central Yupik: A regional overview for the Yukon-Kuskokwim Delta, northern
858 Bristol Bay, and Nunivak Island, Arctic Anthropology, 234-246, http://www.jstor.org/stable/40316467, 1998.

859 Virkkala, A., Aalto, J., Rogers, B. M., Tagesson, T., Treat, C. C., Natali, S. M., Watts, J. D., Potter, S., Lehtonen, A.
860 and Mauritz, M.: Statistical upscaling of ecosystem CO2 fluxes across the terrestrial tundra and boreal domain:
861 Regional patterns and uncertainties, Global Change Biol., 27, 4040-4059, https://doi.org/10.1111/gcb.15659, 2021.

862 Veraverbeke, S., Rogers, B. M. and Randerson, J. T.: Daily burned area and carbon emissions from boreal fires in
863 Alaska, Biogeosciences, 12, 3579-3601, https://doi.org/10.5194/bg-12-3579-2015, 2015.

864 Veraverbeke, S., Delcourt, C. J., Kukavskaya, E., Mack, M., Walker, X., Hessilt, T., Rogers, B. and Scholten, R. C.:
865 Direct and longer-term carbon emissions from arctic-boreal fires: a short review of recent advances, Current
866 Opinion in Environmental Science & Health, 23, 100277, https://doi.org/10.1016/j.coesh.2021.100277, 2021.

867 Veraverbeke, S., Rogers, B. M., Goulden, M. L., Jandt, R. R., Miller, C. E., Wiggins, E. B. and Randerson, J. T.:
868 Lightning as a major driver of recent large fire years in North American boreal forests, Nature Climate Change, 7,
869 529-534, https://doi.org/10.1038/nclimate3329, 2017.

870 Walker, X. J., Baltzer, J. L., Bourgeau-Chavez, L. L., Day, N. J., De groot, W. J., Dieleman, C., Hoy, E. F.,
871 Johnstone, J. F., Kane, E. S. and Parisien, M. A.: ABoVE: Synthesis of Burned and Unburned Forest Site Data, AK
872 and Canada, 1983-2016, ORNL DAAC, https://doi.org/10.3334/ORNLDAAC/1744, 2020.

873 Walker, X. J., Rogers, B. M., Veraverbeke, S., Johnstone, J. F., Baltzer, J. L., Barrett, K., Bourgeau-Chavez, L.,
874 Day, N. J., de Groot, W. J. and Dieleman, C. M.: Fuel availability not fire weather controls boreal wildfire severity
875 and carbon emissions, Nature Climate Change, 10, 1130-1136, https://doi.org/10.1038/s41558-020-00920-8, 2020.

876 Walker, X. J., Baltzer, J. L., Bourgeau-Chavez, L., Day, N. J., Dieleman, C. M., Johnstone, J. F., Kane, E. S.,
877 Rogers, B. M., Turetsky, M. R. and Veraverbeke, S.: Patterns of ecosystem structure and wildfire carbon
878 combustion across six ecoregions of the North American boreal forest, Frontiers in Forests and Global Change, 3,
879 87, https://doi.org/10.3389/ffgc.2020.00087, 2020.

880 Walker, X. J., Baltzer, J. L., Cumming, S. G., Day, N. J., Ebert, C., Goetz, S., Johnstone, J. F., Potter, S., Rogers, B.
881 M. and Schuur, E. A.: Increasing wildfires threaten historic carbon sink of boreal forest soils, Nature, 572, 520-523,
882 https://doi.org/10.1038/s41586-019-1474-y, 2019.

883 Walker, X. J., Baltzer, J. L., Cumming, S. G., Day, N. J., Johnstone, J. F., Rogers, B. M., Solvik, K., Turetsky, M. R.
884 and Mack, M. C.: Soil organic layer combustion in boreal black spruce and jack pine stands of the Northwest
885 Territories, Canada, Int. J. Wildland Fire, 27, 125-134, https://doi.org/10.1071/WF17095, 2018a.

886 Walker, X. J., Rogers, B. M., Baltzer, J. L., Cumming, S. G., Day, N. J., Goetz, S. J., Johnstone, J. F., Schuur, E. A.,
887 Turetsky, M. R. and Mack, M. C.: Cross-scale controls on carbon emissions from boreal forest megafires, Global
888 Change Biol., 24, 4251-4265, https://doi.org/10.1111/gcb.14287, 2018b.

889 Ward, D. S., Kloster, S., Mahowald, N. M., Rogers, B. M., Randerson, J. T. and Hess, P. G.: The changing radiative
890 forcing of fires: global model estimates for past, present and future, Atmospheric Chemistry and Physics, 12, 10857-
891 10886, https://doi.org/10.5194/acp-12-10857-2012, 2012.

892 Wiggins, E. B., Veraverbeke, S., Henderson, J. M., Karion, A., Miller, J. B., Lindaas, J., Commane, R., Sweeney,
893 C., Luus, K. A. and Tosca, M. G.: The influence of daily meteorology on boreal fire emissions and regional trace
894 gas variability, Journal of Geophysical Research: Biogeosciences, 121, 2793-2810,
895 https://doi.org/10.1002/2016JG003434, 2016.

896 Zhou, Z., Liu, L., Jiang, L., Feng, W. and Samsonov, S. V.: Using long-term SAR backscatter data to monitor post-
897 fire vegetation recovery in tundra environment, Remote Sensing, 11, 2230, https://doi.org/10.3390/rs11192230,
898 2019.